Tectonophysics 798 (2021) 228685

Contents lists available at ScienceDirect

Tectonophysics

journal homepage: www.elsevier.com/locate/tecto

Three-dimensional numerical simulation of the interseismic and coseismic phases associated with the 6 April 2009, M_w 6.3 L'Aquila earthquake (Central Italy)

Matteo Albano [a,*], Salvatore Barba [a], Christian Bignami [a], Eugenio Carminati [b], Carlo Doglioni [a], Marco Moro [a], Salvatore Stramondo [a], Michele Saroli [c,a]

[a] Istituto Nazionale di Geofisica e Vulcanologia, via di Vigna murata 605, 00143 Roma, Italy
[b] Dipartimento di Scienze della Terra, "Sapienza" Università di Roma, Piazzale Aldo Moro 5, 00185 Roma, Italy
[c] Dipartimento di Ingegneria Civile e Meccanica, Università degli Studi di Cassino e del Lazio meridionale, via G. di Biasio 43, 03043 Cassino (FR), Italy

ARTICLE INFO

Keywords:
L'Aquila earthquake
Numerical model
Gravitational force
Tectonic force
Dilatancy
Coulomb stress
InSAR

ABSTRACT

Although several observations have been reported in the literature before a strong earthquake, their relation with the forthcoming event is often controversial. Since many physical processes and parameters govern the dynamics of preparation, initiation, and occurrence of earthquakes, their understanding is essential for explaining anomalous seismological, geophysical, hydrological and geodetic signals before a strong earthquake that may be considered for seismic monitoring and hazard assessment.

In this work, the interseismic and coseismic stress and strain fields associated with the 6 April 2009, M_w 6.3 L'Aquila earthquake are calculated via a 3D numerical model designed to simulate the crustal interseismic loading and the coseismic brittle episodic dislocation along the fault. The model adopts a framework of gravitational and tectonic forces that are compatible with the geodynamics of the Central Apennines region of the Italian territory. The model assumes a brittle upper crust, where the fault has stick-slip behaviour, and a plastic deeper crust, where the fault is in stationary creep.

The results indicate that the concurrent action of gravitational and tectonic forces determines steep interseismic stress gradients at the transition between the creeping and locked fault planes that promote the coseismic subsidence of the hanging wall. The interseismic strain above the transition between that locked upper fault and its unlocked lower shear zone develops a dilated volume in the hanging wall and a contracted volume in the footwall. These stress and strain variations are compatible with seismological, geophysical and geodetic anomalies observed before the earthquake, i.e., V_p/V_s anomalies and location of foreshocks. Interseismic stress and strain patterns invert during the coseismic stage. The dilated volume, formed during the interseismic phase, will be contracted at the coseismic stage and, conversely, the footwall volume previously contracted will be expanded.

1. Introduction

Earthquakes are the result of stress and strain accumulation in the Earth's crust over variable (decade to millennial) periods, which is followed by a sudden stress release at a crustal discontinuity (Scholz, 2019). Earthquake nucleation depends on several physical processes that are often difficult to model. Several phenomena, such as seismicity patterns, changes in b-value, aseismic deformation-rate changes, seismic velocity changes, modifications of hydrological and geochemical parameters, and changes in the electrical and magnetic field have been sometimes observed before strong earthquakes (Bouchon et al., 2013; Cicerone et al., 2009; Crampin et al., 2015; Hartmann and Levy, 2005; Mavrommatis et al., 2014; Ohtake et al., 1981; Roeloffs, 1988; Schurr et al., 2014). However, their relationship with the upcoming earthquake is controversial. Some phenomena may be related to the beginning of processes associated with the earthquake nucleation or may indicate a general advanced state of the loading cycle. Also, other phenomena are observed, but their occurrence in the vicinity of and sometimes before

* Corresponding author.
E-mail address: matteo.albano@ingv.it (M. Albano).

https://doi.org/10.1016/j.tecto.2020.228685
Received 18 July 2020; Received in revised form 3 November 2020; Accepted 13 November 2020
Available online 21 November 2020
0040-1951/© 2020 Published by Elsevier B.V.

the occurrence of an earthquake is a mere coincidence (Scholz, 2019).

Understanding the physical processes that can precede earthquakes is mandatory to correctly identify geophysically observable phenomena and eventually use them for forecasting purposes. This work aims at understanding the physical processes related to the nucleation of the M_w 6.3 L'Aquila earthquake (hereinafter L'Aquila 2009) that happened in Central Italy on 6 April 2009 (Fig. 1a). The earthquake occurred along the Central Apennines belt, which is characterized by extensional tectonics, with normal faulting mainly confined in the upper crust (Carminati and Doglioni, 2012; Galadini et al., 2012; Chiarabba et al., 2015), and nucleated approximately 4 km southwest of the city of L'Aquila, at a depth of approximately 9 km (Valoroso et al., 2013) (Fig. 1b). The earthquake dislocated the Paganica fault, a normal fault trending NW-SE and dipping 45 to 50 degrees to the SW (Atzori et al., 2009; Castaldo et al., 2018; Falcucci et al., 2009; Gori et al., 2012; Trasatti et al., 2011; Volpe et al., 2012). The mainshock was followed by a 3-year-long aftershock sequence comprising more than 80,000 events that occurred within a 35-km-long NW-SE-trending area (Fig. 1b) (Chiaraluce et al., 2011; Valoroso et al., 2013).

Several a-posteriori studies identified some seismological, geophysical and geodetic signals in the days to months before the event. A cluster of small foreshocks occurred nearby the mainshock hypocentre in the previous six months. These events (blue dots in Fig. 1b) started on a narrow band of the deepest portion of the NW-SE trending and SW dipping main fault, then switched on an antithetic plane, NW-SE trending and NE dipping, where an M_w 4.0 foreshock occurred on 30 March 2009. In the last week before the mainshock, the seismicity switched again to the mainshock rupture plane (Chiaraluce et al., 2011). Fluctuations in the b-value were also reported in the months before the mainshock, reflecting increasing stress due to fracture growth on a local patch of the fault before the mainshock rupture (De Gori et al., 2012; Sugan et al., 2014; Gulia et al., 2016). Changes in the V_P/V_S ratio and anisotropy parameters were also observed from January 2009 (Baccheschi et al., 2019; Di Luccio et al., 2013; Lucente et al., 2010). Additionally, GPS and InSAR data identified specific patterns of ground deformation in the vicinity of the epicentral area. An analysis of continuous GPS stations identified a transient signal, which was attributed to a slow slip event that originated beneath the reactivated normal faulting system (Borghi et al., 2016). Multitemporal analysis of Interferometric Synthetic Aperture Radar data (InSAR) identified a preseismic broad signal of unclear origin (Atzori et al., 2013). Another InSAR study identified subsidence acceleration, starting three years before the earthquake, in two Quaternary sedimentary basins (located north-west of the main fault), that experienced about 10–15 mm of subsidence (Moro et al., 2017).

The occurrence of most of these observations has been interpreted in the framework of the dilatancy-diffusion conceptual model (Nur, 1972; Scholz, 1974). This model assumes that dilatancy occurs within a stressed volume surrounding an impending rupture zone and evolves at an accelerating rate, potentially involving the development of pore

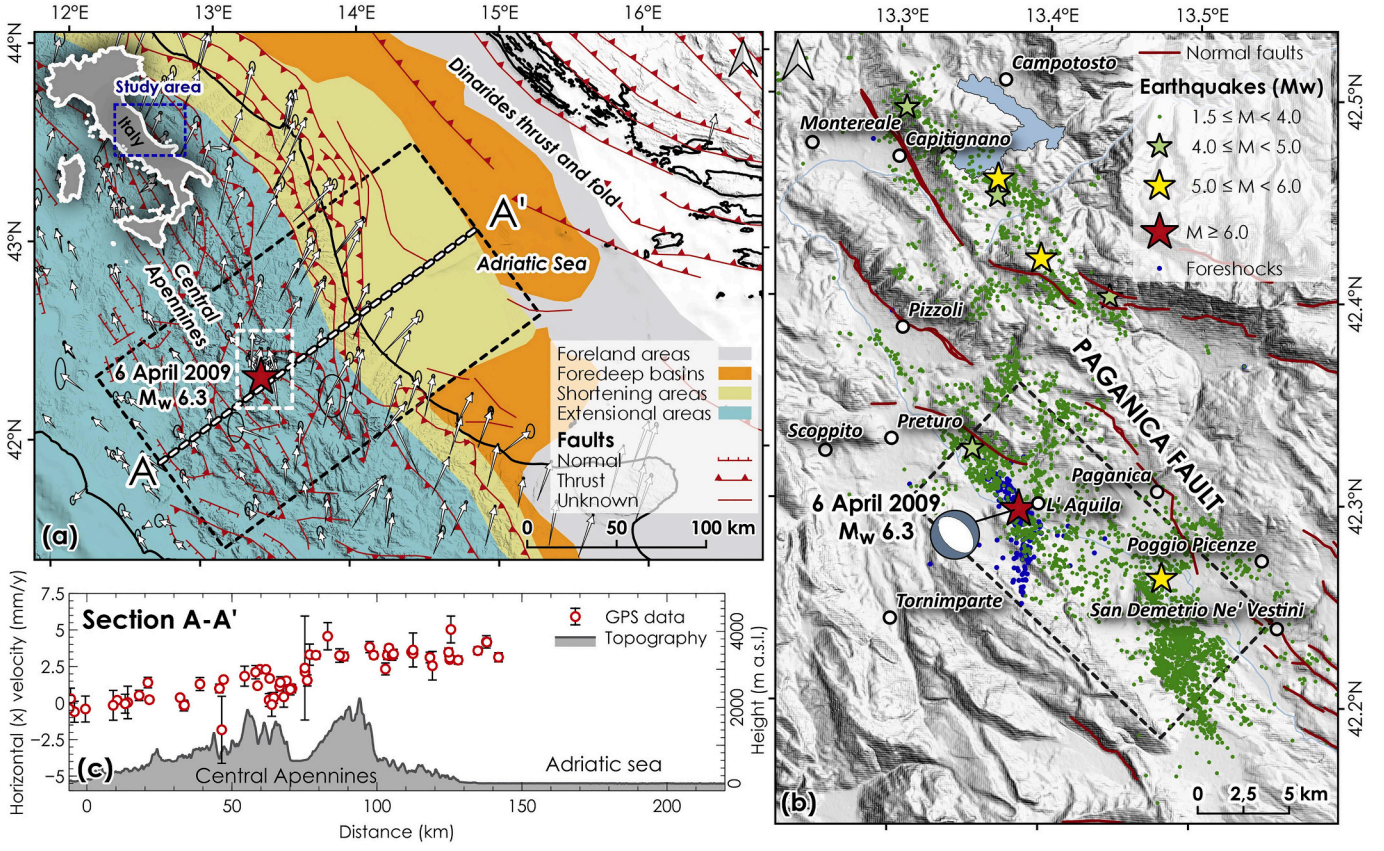

Fig. 1. Sketch of the study area. (a) Simplified tectonic map showing the main tectonic and geodynamic setting of the region (modified from Carminati and Doglioni (2012) and Petricca et al. (2015)) with the locations of the L'Aquila 2009 event and the footprint of panel b (the dashed white rectangle). The white arrows identify the interseismic horizontal velocities at GPS sites to a fixed Eurasian frame (with 95% error ellipses (Devoti et al., 2017)). The dashed black rectangle indicates the footprint of the 3D numerical model of Fig. 3. (b) The L'Aquila 2009 seismic sequence (Chiaraluce et al., 2011; Valoroso et al., 2013), showing the location of the mainshock (the red star) and the aftershocks, classified according to the magnitude. The blue dots indicate the position of the earthquakes ($M_w \leq 4.0$) registered six months before the mainshock. The black rectangle indicates the projection at the surface of the fault plane responsible for the event, estimated from the analytical inversion of geodetic data (Atzori et al., 2009). (c) Plot of the horizontal velocities from GPS stations enclosed in the dashed black rectangle in panel a, projected along the cross-section A-A', together with the topographic profile. (For interpretation of the references to colour in this figure legend, the reader is referred to the web version of this article.)

pressure changes and the diffusion of highly pressurized fluids, like groundwater or CO_2 overpressurized reservoirs (Chiodini et al., 2004), which triggered the mainshock. Although many works share this view, none of them provided a quantitative characterization of the interseismic crustal dynamics and the potential stress and strain field (Lucente et al., 2010; Moro et al., 2017; Savage, 2010; Sugan et al., 2014; Terakawa et al., 2010).

In this work, we focused on quantifying stress and strain variations at depth and discussing how they relate to the occurrence of the mainshock. To this purpose, we developed a first-order, crustal-scale 3D static numerical model to jointly simulate the long-term crustal interseismic loading and the coseismic brittle episodic dislocation associated with the L'Aquila 2009 earthquake. The model assumes a framework of gravitational and tectonic forces that is compatible with the geodynamics of the Central Apennines region of the Italian territory. Here, the fault dislocates under the effect of the internal stress and strain field, which are the result of the applied far-field boundary conditions, forces, and rheological behaviour of geomaterials. Differently from kinematic models, in which the fault slip is the forcing term and is determined to fit the coseismic data, the static forward model can help to quantify the stress and strain changes before earthquake nucleation.

The results of our physical model provide a quantitative picture of the interseismic stress and strain pattern at seismogenic depth before the earthquake nucleation. Modelling of the interseismic phase shows evidence of interseismic dilatancy at depth in the hanging wall, in a volume embedding the L'Aquila 2009 earthquake, while volumetric contraction develops in the footwall. In terms of stresses, interseismic Coulomb stress changes promote the coseismic dislocation of the fault responsible for the L'Aquila 2009 mainshock. Such stress and strain changes provide a quantitative description for the seismological, geophysical and geodetic phenomena observed before the mainshock.

2. Methods

2.1. Conceptual scheme and numerical model

The stress, strain and displacement fields associated with the interseismic and coseismic phases of the L'Aquila 2009 earthquake were simulated by assuming a first-order conceptual scheme that presents a simple fault plane cross-cutting a medium composed of a brittle upper crust and a plastic lower crust (Fig. 2). We speculate that the fault has two different slip styles along the dip direction, i.e., an episodic stick-slip behaviour along its brittle upper part (representing an asperity), and steady-state shear (creep) behaviour along its deeper part (Scholz, 2019). In the interseismic phase (Fig. 2a), the presence of the gravitational force ensures that the stress tensor is compressive at every depth in the crust. However, the presence of extensional tectonic loads gradually reduces the horizontal stresses. The different behaviour of the locked upper part of the fault concerning the viscous shearing of its plastic lower part generates extensional stress and strain gradients in a crustal volume of the hanging wall at the brittle-plastic transition, antithetic to the main fault plane (Fig. 2a) (Doglioni et al., 2011, 2014, 2015). This model also applies for normal faults forming above a shallow dip basal decollement within the brittle upper crust, as in the M_w 6.5 Amatrice-Norcia 2016 seismic sequence (Bignami et al., 2019). A dilated volume may gradually develop during the interseismic period, creating a volume weakened by fracturing that, depending on the tectonic loading-rate, the relative permeability of the rock, and the presence of sealing barriers, could involve the development of pore fluid pressure gradients, fluid migration, as well as changes in physical properties of the rock (Lucente et al., 2010; Doglioni et al., 2014).

The interseismic stress and strain gradients promote the coseismic dislocation of the upper fault plane, thus dissipating the accumulated stress and strain by the rapid downward movement of the hanging wall and recovering the dilated volume at depth (Fig. 2b).

We exploited this conceptual scheme to simulate the interseismic and

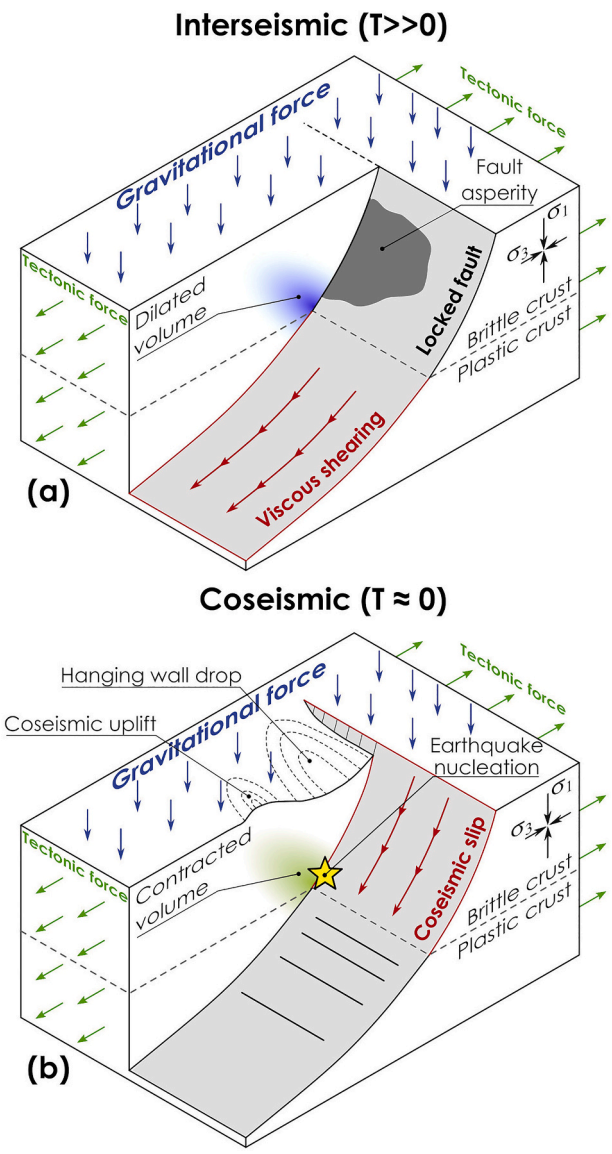

Fig. 2. Isometric view of the first-order conceptual sketch explaining the interseismic (a) and coseismic (b) phases for the L'Aquila 2009 normal-fault earthquake (modified from Doglioni et al. (2011, 2014, 2015). The figure shows only half of the conceptual model. The symmetric half and part of the hanging wall are hidden for representation purposes.

coseismic phases of the L'Aquila 2009 earthquake in the framework of the geodynamic setting of the Central Apennines (Fig. 1a), dominated by the W- and SW-ward subduction of the Adriatic plate and *E*- and NE-ward retreat of the subduction hinge, relative to the upper European plate. This geodynamic setting generates contraction and the generation of the accretionary prism in the frontal part of the belt (the western Adriatic Sea) and contemporaneous extension in the backarc area all along the Apennines belt and the Tyrrhenian Sea (Doglioni, 1991). From the Late Eocene-Oligocene to present time, the Apennines fold-and-thrust belt was characterized by the eastward (in the Central and Southern Apennines) migration of thrust fronts (Malinverno and Ryan, 1986; Patacca et al., 1990). To the east, the Adriatic margin served as the foreland to the migrating thrust belt. Starting in the Late Miocene, extensional tectonics, associated with backarc rifting, dissected the Apennines by high-angle normal and oblique faulting, which cut through the pre-existing compressional structures (Ferranti and Oldow, 1999; Hippolyte et al., 1994) and progressively migrated from the western to the eastern parts of the orogen (Malinverno and Ryan, 1986;

Patacca et al., 1990; Westaway, 1990; Doglioni, 1991; Amato and Montone, 1997). Nowadays, the accretionary prism is still active, and thrusting is currently active on the Adriatic side of the Central Apennines, as indicated by seismicity, deformation of Quaternary sediments, and GPS data (Fig. 1a) (Cuffaro et al., 2010; Palano, 2015; Livani et al., 2018). Thrusting is also active along the Dinarides belts, where the Adriatic plate subducts ENE-ward beneath Eurasia (Fig. 1a) (Kastelic and Carafa, 2012).

This geodynamic context has been simulated with a 3D finite element numerical model, built with the commercial code MSC Marc 2018 (MSC Software Corporation, 2018), which encompasses a broad area, including most of the Central Italy Apennine chain and the Adriatic Sea offshore (dashed black rectangle in Fig. 1a). One of the most challenging tasks in tectonic modelling is the definition of appropriate model dimensions and boundary conditions. The simulation of the L'Aquila earthquake is performed adopting the setting used in previous numerical models of the interseismic deformation in central Italy (Barba et al., 2010, 2008; Candela et al., 2015; Finocchio et al., 2016, 2013). Such models were expanded to include the coseismic dislocation scheme proposed by Doglioni et al. (2011). The model (Fig. 3) extends 220 km in the NE-SW (x-direction in Fig. 3) and 120 km in the NW-SE (z-direction in Fig. 3), for a depth of 40 km. The model bottom is fixed along the vertical direction, while the upper boundary is free to move (Fig. 3). The lateral boundaries present roller constraints that lock the horizontal movements orthogonally to the model sides. Such a choice agrees with the interseismic horizontal velocity vectors from GPS (Fig. 1c) (Devoti et al., 2017), which show that the horizontal interseismic ground motion is approximately SW-NE of the model (the x-direction in Fig. 3) and is negligible along the NW-SE direction (the z-direction in Fig. 3). Moreover, an approximately zero-velocity area corresponds to the SW model boundary (Fig. 1c), which agrees with the assumed horizontal fixity. The NE boundary of the model is constrained by considering that the Adriatic domain is undergoing compression (Fig. 1a) and that the horizontal strain-rate and velocity in the middle of the Adriatic sea offshore is almost negligible (Carafa et al., 2015; Pezzo et al., 2020). Thus, the location of the NE model boundary is set at approximately 80–90 km offshore, roughly equidistant from the Apennines and Dinarides thrust fronts.

The applied forces consist of the gravitational force (green arrows in Fig. 3) and uniform shear tractions at the model base (blue arrows in Fig. 3), directed towards the NE and parallel to the x-direction of the model. The latter simulates the basal shear traction exerted by the eastward mantle flow associated with the rollback of the Adriatic slab and has been successfully adopted to simulate the active tectonic deformation in the Central Mediterranean (Barba et al., 2008, 2010; Candela et al., 2015; Finocchio et al., 2013, 2016). Basal shear tractions, together with the horizontal constraints at the SW and NE model sides, enable a first-order description of the ongoing crustal interseismic stretching of the Central Apennine chain and the compression of the Adriatic offshore (Fig. 1a) (Doglioni, 1991; Doglioni et al., 1999; Carafa and Bird, 2016).

The finite-element mesh is composed of eight-node hexahedral elements, with their size ranging from approximately 0.3 km on the fault trace to 5–10 km at the bottom and sides of the model. The model presents a discontinuity in the mesh, indicated by the green (No. 1) and red (No. 2) planes in Fig. 3, which is intended to simulate the L'Aquila 2009 earthquake causative fault plane. The fault presents a strike and dip of approximately 130° and 47°, respectively (Atzori et al., 2009), and is composed by two subplanes that simulate the steady-shearing (No. 1 in Fig. 3) and stick-slip behaviour (No. 2 in Fig. 3) of the fault. The fault extent at depth is limited to approximately 15 km because of the presence of a decollement level, i.e., the Latium-Abruzzi extensional detachment (Lavecchia et al., 2017), which delimitates the SW dipping intra-Apennines active faults of Central Italy. The transition between the brittle and plastic behaviour of the fault plane is at approximately 10 km depth, according to the location of the hypocentres of the foreshocks and the mainshock (Chiaraluce et al., 2011; Valoroso et al., 2013). Therefore, the red (No. 2) and green (No. 1) segments present an along-dip length of approximately 12 km (D1) and 8 km (D2), respectively. The fault behaviour is modelled assuming a frictional contact interface between the two walls of the discontinuity, where the nodes are doubled so that the footwall and the hanging wall of the fault can move relative to each other, according to the Mohr-Coulomb failure criterion:

$$\tau = -\sigma\mu \quad (1)$$

where τ is the shear stress, σ is the normal stress (assumed positive when tensile), and μ is the friction coefficient.

Unlike conventional kinematic models, no forces or displacements are imposed on the fault edges (No. 1 and 2 in Fig. 3) to induce slip. Instead, the walls of the fault plane are assumed alternatively locked or unlocked in space and time (Doglioni et al., 2011, 2014). No self-consistent failure criterion, e.g., rate-and-state friction (Ruina, 1983; Aharonov and Scholz, 2018), is assumed on the fault plane, but the timing of fault rupture is imposed a-priori. In detail, the locked and unlocked condition is attained by manually changing the friction coefficient at the interface. In case of a locked fault, the friction coefficient assumes a large value, i.e., 0.7 (Byerlee, 1978) to avoid the relative movement between the nodes belonging to the footwall and hanging wall. In case of an unlocked fault, friction is set to a low value (0.05) (Di Toro et al., 2011) to simulate the interseismic viscous sliding of the deep fault segment (No. 1 in Fig. 3) and the coseismic dislocation of the upper fault segment (No. 2 in Fig. 3). When unlocked, nodes along the fault

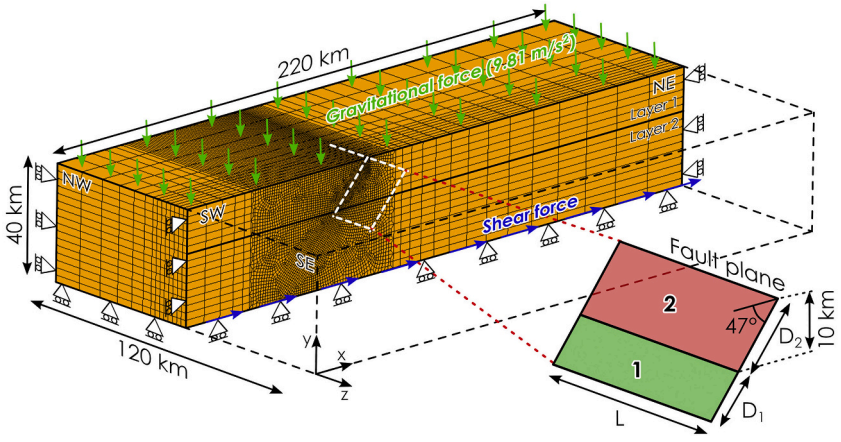

Fig. 3. 3D finite element geometry, mesh, and boundary conditions developed for the simulation of interseismic and coseismic phases associated with the L'Aquila 2009 earthquake. The figure shows only half of the conceptual model. The symmetric half is hidden for representation purposes.

edges move each other under the drive of the applied far-field boundary conditions, forces, and internal stress. This approach allows investigating the different stress and strain distributions associated with the interseismic and coseismic phases, rather than assessing what processes control the timing of rupture.

A linear elastic isotropic model describes the evolution of stress and strain within the medium. The complex geology of the study area is simplified into two layers (Fig. 3). Such a simplification is consistent with the first-order nature of the performed modelling. The elastic and state parameters come from literature data and geophysical measurements available over the study area (Carannante et al., 2013). The assumed values are reported in Table 1 and are consistent with those adopted in related case studies in Italy (Trasatti et al., 2011; Albano et al., 2015; Finocchio et al., 2016; Castaldo et al., 2018; Tung and Masterlark, 2018).

2.2. Simulation phases and model validation

Simulations present an interseismic phase and a coseismic phase. The mechanical boundary conditions are activated at the beginning of the analysis, while the applied forces and locking status for the fault segments are specified in Table 2 for each phase.

The interseismic phase mimics the accumulation of the long-term pre-earthquake stress and strain field in the crust resulting from the applied gravitational and basal shear forces and boundary conditions. The analysis type is elastic and lasts for one loading step, within a single numerical increment. In this way, the viscoelastic behaviour of the lower crust is neglected, thus focusing on the cumulated interseismic stress and strain field only, rather than assessing the shape of the loading path. This phase presents two sub-stages. In the first stage, the model self-consolidates under gravity only (green arrows in Fig. 3). Both the fault surfaces are unlocked (No. 1 and No. 2 in Table 2 and Fig. 3) so that the footwall and the hanging wall can move relative to each other, accommodating the lithostatic load. In the second stage, the basal shear tractions are activated (blue arrows in Fig. 3) to simulate the interseismic tectonic loading. The deep fault plane is kept unlocked (No. 1 in Fig. 3) to simulate a fault that steadily shears during the interseismic phase (Doglioni et al., 2011; Scholz, 2019), while the upper fault plane is locked (No. 2 in Fig. 3) to simulate a fault asperity during the tectonic loading.

Notice that in extensional tectonic settings, the state of stress within the crust is always compressive below about 1 km due to the confining pressure exerted by the lithostatic load. In other words, as classically depicted by the state of stress in extensional settings, the maximum stress (σ_1) is vertical, and the minimum stress (σ_3) is horizontal but still positive (i.e., contractional) beneath 1 km depth (Bignami et al., 2020). Therefore, the stress determining the activation of the downward motion of the hanging wall volume is given by the lithostatic load (i.e., gravity). For these basic observations, the normal faulting cannot be considered as generated by an elastic rebound, but rather by the gravitational collapse of the hanging wall (Bignami et al., 2020). Due to this difference, Doglioni et al. (2015) proposed the nomenclature of graviquakes for normal-fault earthquakes.

The coseismic phase lasts for one loading step within a single numerical increment to calculate the coseismic deformation induced by the unlocking the upper fault plane (No. 2 in Fig. 3), while the lower fault plane (No. 1 in Fig. 3) is locked. Both the mechanical boundary conditions and forces applied in the interseismic phase are still active in this phase.

Table 1
Parameters adopted in the numerical analysis.

Parameter	Description	Layer 1	Layer 2
ρ (kg/m^3)	Mass density	2600	2600
ν	Poisson's ratio	0.3	0.25
E (GPa)	Young modulus	20	35

Table 2
Applied forces, type of analysis, and locking status of faults for each modelling phase. For the location of the fault surfaces, see Fig. 3.

Modelling phase	Analysis type	Applied forces	Fault segments (L = locked; U = unlocked)	
			No. 1	No. 2
Interseismic	Elastic	Gravity force	U	U
		Basal shear traction	U	L
Coseismic	Elastic	Gravity + basal shear	L	U

Preliminary models highlight that stress, strain, and ground displacements in interseismic and coseismic phases rely on the magnitude of the applied basal shear traction and the extent of the locked and unlocked portions of the fault plane. Otherwise, the rheological properties of the medium play a minor role (Doglioni et al., 2014). Therefore, the model performance has been established by carrying on a trial-and-error procedure with a parametric analysis to search for the combination of the amplitude of the applied shear traction (blue arrows in Fig. 3) and the along-strike length of locked and unlocked fault planes (L in Fig. 3) that fits the coseismic ground displacements observed with the interferometric synthetic aperture radar (InSAR) technique.

The quality of the modelled solution is then evaluated by estimating the root mean square error (RMSE) of the residuals between the observed and modelled displacements, expressed as follows:

$$RMSE = \sqrt{\frac{1}{N}\sum_{i=1}^{N}\left(y_{i,obs} - y_{i,mod}\right)^2} \quad (2)$$

where $y_{i,obs}$ and $y_{i,mod}$ are the observed and modelled displacements of the ith points and N the number of points.

2.3. InSAR data and processing

The coseismic displacements caused by the earthquake have been investigated with InSAR data from the ENVISAT satellite mission. Pre- and post-event images were acquired on 11 March and 15 April 2009 along the ascending orbit, and on 20 July 2007 and 12 April 2009 along the descending orbit. The ascending and descending unwrapped coseismic interferograms are computed by applying the classical InSAR technique (Massonnet and Feigl, 1998) using the GAMMA© SAR software package (Wegmuller et al., 1998). The topographic phase has been removed from the interferograms by using the SRTM 1-arc sec Digital Elevation Model (Farr et al., 2007), while phase noise filtering (Goldstein and Werner, 1998) has been applied to the wrapped interferograms using the Minimum Cost Flow algorithm (Costantini, 1998). A multilook factor has been applied to achieve a final ground pixel resolution of about 30 m, in agreement with the SRTM resolution cell.

3. Results

The description of the results of the numerical simulations refers to the best-fit model. They are presented in terms of differential displacement, stress, and strain fields in the interseismic and coseismic phases, respectively.

3.1. Interseismic phase

At the end of the interseismic phase, the lithostatic load produces horizontal and vertical stress distributions that increase almost linearly with depth and are compressive at every depth in the model.

The basal shear tractions, with an amplitude of approximately 1.6 MPa, modify the horizontal stress and strain field along the x-direction. In detail, the SW part of the model experiences horizontal stress relaxation and extension (Fig. 4a and b), while the NE part experiences stress

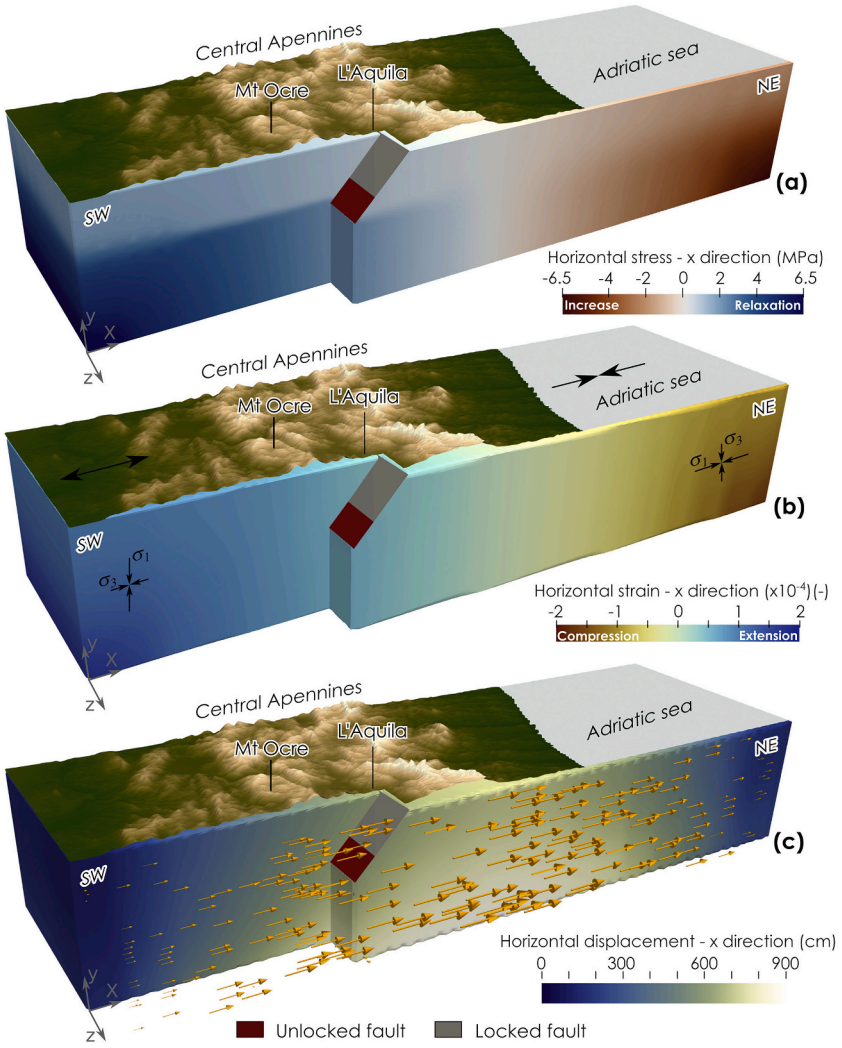

Fig. 4. Effect of the interseismic basal shear tractions only (i.e., excluding the contribution of the gravity force) for the L'Aquila 2009 earthquake model. a) Modelled differential stress field along the x-direction. b) Modelled differential horizontal strain field along the x-direction. c) Modelled differential horizontal displacement pattern and vectors (orange arrows) along the x-direction. The figure shows only half of the numerical model. The symmetric half along the z-direction is hidden for representation purposes.

increase and contraction. Such stress and strain changes adequately simulate the tectonic stretching of the Central Apennines area and the compression of the Adriatic offshore (Fig. 1a). The fault plane that simulates the L'Aquila 2009 earthquake (red and grey planes in Fig. 4) is located in an extensional tectonic field.

The resulting horizontal displacement along the x-direction (Fig. 4c) is NE-directed (orange arrows) and is constant along the z-direction. Horizontal movements are null at the model sides because of the assumed horizontal constraints, then gradually increase towards the centre, with a maximum value of approximately 900 cm.

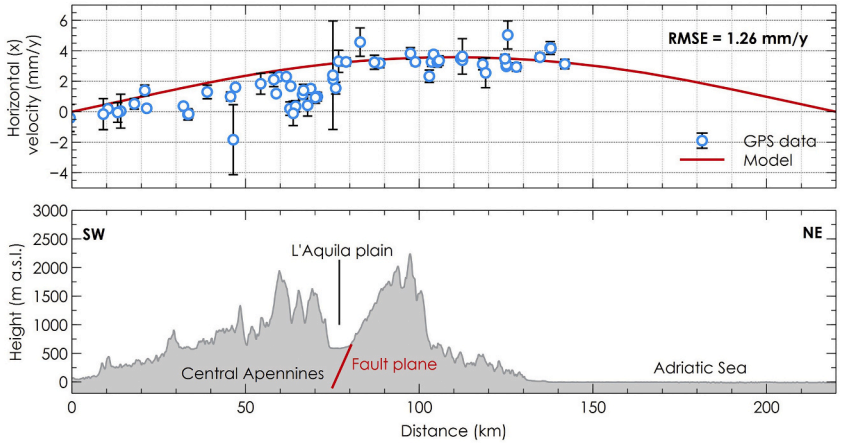

Fig. 5. Comparison between observed (light blue circles) and modelled (red curve) interseismic horizontal ground velocities along the x-direction (Fig. 3) in the median part of the model. The RMSE is calculated according to Eq. (2). (For interpretation of the references to colour in this figure legend, the reader is referred to the web version of this article.)

The modelled interseismic horizontal displacements at the ground surface along the x-direction (Fig. 4c) were scaled relative to time and compared with the horizontal interseismic ground velocities from GPS data (Fig. 1a and c). Fig. 5 shows the comparison between the calculated equivalent horizontal velocity profile at the ground level along the A-A' cross-section in Fig. 1a (red curve) and the horizontal velocities from the GPS stations (blue circles) comprised by the model footprint in Fig. 1a, and projected along the x-direction, together with 1-σ confidence error bars. Assuming a time factor of approximately 1900 years yields a fair fit between the observed and modelled velocities, with an RMSE of about 1.3 mm/year. The spatial long-wavelength velocity trend of the GPS data is well captured by the model, which adequately reproduces the nearly NE-directed GPS velocity increase in the Central Apennines and the maximum GPS velocity. However, the homogenous model does not capture short-wavelength velocity variations in the GPS data. These are likely associated with geometrical and rheological heterogeneities in the upper crust (Finocchio et al., 2016).

At the brittle-plastic transition (i.e., at the transition between the locked and unlocked fault planes), the interseismic shearing of the deep fault plane (the plane No. 1 in Fig. 3) determines a rotation of stress and strain axes. The interseismic displacement pattern and vectors (Fig. 6a), cleared of the large-scale interseismic displacements of Fig. 4c, show the interseismic normal dislocation of the lower fault plane. Displacements are SE-directed and reach maximum values close to the shearing fault, while gradually reduce moving aside. A small amount of deformation is also detected at the ground level. Such interseismic displacements induce dilation at depth in the hanging wall, at the transition between the locked and unlocked fault planes (positive volumetric strains in Fig. 6b), while volumetric contraction develops in the shallow most two-kilometre of the hanging wall because of the interseismic ground subsidence caused by the shearing of the deep fault plane, and in the footwall because of its mainly NE-ward movement (negative values in Fig. 6b).

Stress variations, expressed in terms of Coulomb stress changes (ΔCFS) (Fig. 6c), calculated along preferential NW-SE trending planes dipping 47° towards SW (corresponding to the dip of the segment No. 2

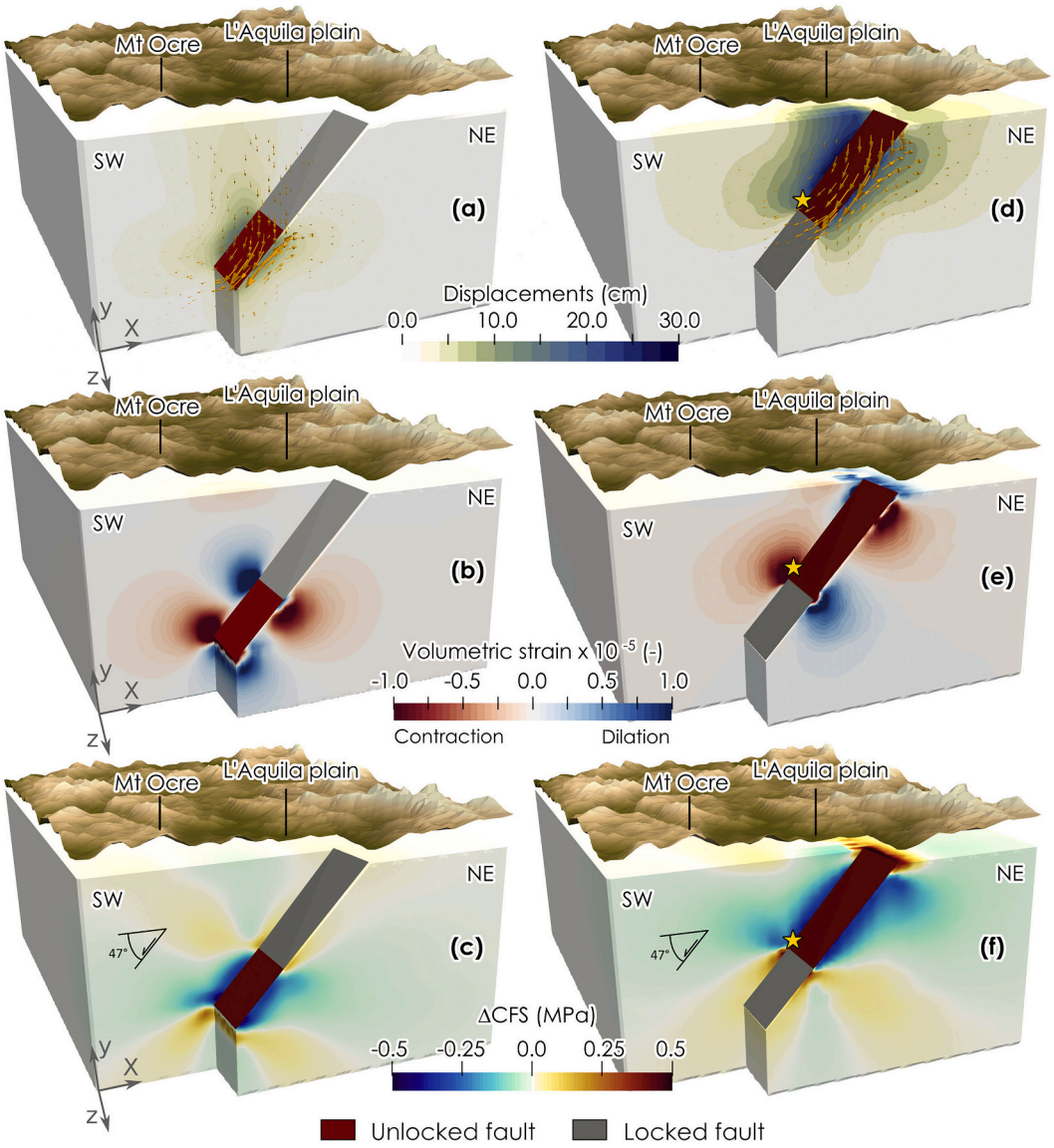

Fig. 6. Modelling results at the end of the interseismic and coseismic phases. a) Interseismic differential displacements and vectors (orange arrows), b) volumetric strain, and c) ΔCFS caused by the interseismic shearing of the deep fault plane (No. 1 in Fig. 3). d) Coseismic differential displacements and vectors (orange arrows), e) volumetric strain, and f) ΔCFS caused by the coseismic dislocation of the upper fault plane (No. 2 in Fig. 3). The yellow star in panel d, e, and f indicates the approximate position of the mainshock at depth. The figure shows only half of the numerical model. The symmetric half in the z-direction is hidden for representation purposes. (For interpretation of the references to colour in this figure legend, the reader is referred to the web version of this article.)

in Fig. 3) and with μ = 0.6 (Byerlee, 1978), show that the locked fault segment falls within a positive ΔCFS volume, where extensional earthquakes are promoted.

3.2. Coseismic phase

In the coseismic phase, the earthquake dislocation occurs by unlocking the shallower part of the fault (No. 2 in Fig. 3). The coseismic deformation pattern (Fig. 6d) highlights the down and SW-ward movement of the hanging wall and the mainly NE-ward movement of the footwall, consistently with geodetic observations and analytical or numerical models (Atzori et al., 2009; Trasatti et al., 2011). The coseismic fault slip is directed downdip (Fig. S1) with maximum values of approximately 90 cm reached about 6–10 km at depth. The geodetic moment tensor computed from the retrieved slip distribution, the fault area and the stiffness, is about 1.61 × 10^{18} Nm, corresponding to a magnitude of approximately 6.1. The coseismic dislocation induces the volumetric contraction of the hanging wall at the brittle-plastic transition (Fig. 6e), thus recovering the volumetric dilation accumulated in the interseismic phase (Fig. 6b). A complex pattern of dilated and compressed volumes occurs in the shallow most 1–2 km due to the combination of subsidence and south-westward movement of the hanging wall. Conversely, the footwall experiences dilation at the brittle plastic transition that relaxes the interseismic volumetric contraction, while contraction develops in the upper part because of the mainly horizontal movement of footwall induced by the hanging wall downward movement. The coseismic ΔCFS pattern (Fig. 6f) shows increasing stresses at the fault tips and is consistent with those calculated with conventional analytical approaches (Serpelloni et al., 2012).

The modelled coseismic displacements at the ground level (Fig. 6d) have been projected along the ascending and descending line of sight (LOS) of the ENVISAT satellites and compared with the corresponding InSAR observations. The InSAR-derived displacement pattern (Fig. 7a), showing the predominant subsidence of the hanging wall (negative values) and the mainly eastward movement of the footwall (positive values), is well resolved by the model (Fig. 7b). Indeed, the residuals between modelled and measured displacements (Fig. 7c) are less than 3 cm. At the same time, the computed RMSE is less than 10% of the maximum observed displacements, and it is comparable with the results of finite-fault dislocation models available in the literature (Atzori et al., 2009; Trasatti et al., 2011).

4. Discussion

The proposed numerical approach allowed us to model the interseismic and the coseismic phases associated with the L'Aquila 2009

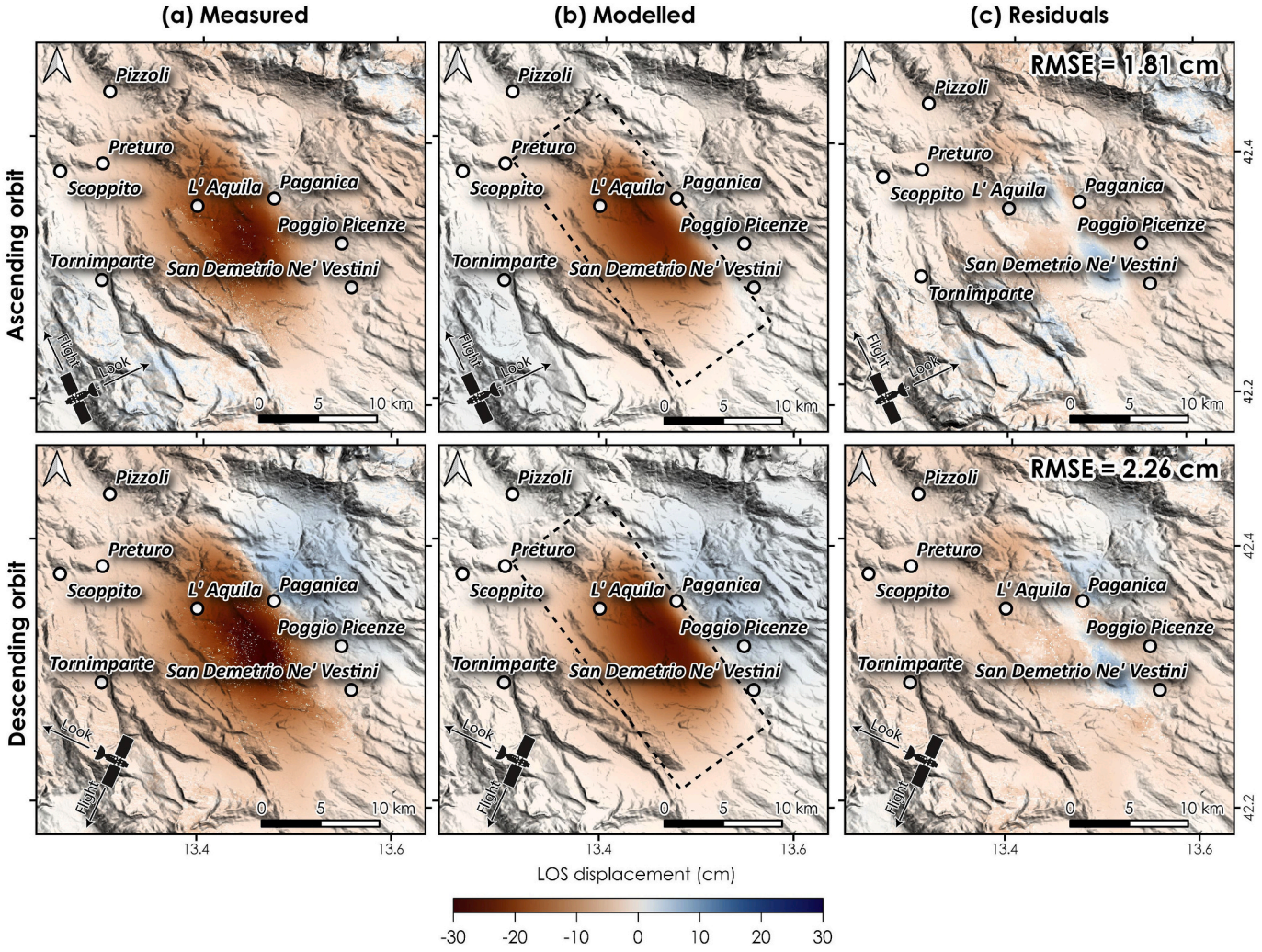

Fig. 7. Comparison between measured and modelled coseismic displacements. a) Coseismic ground displacement field from InSAR data along the ascending and descending orbits, associated with the L'Aquila 2009 earthquake. Positive and negative values indicate ground movements towards and away from the satellite sensor, respectively. b) Modelled LOS displacements. The dashed black rectangle identifies the projection at the surface of the modelled fault. c) Residuals between the modelled and observed LOS displacements. The RMSE is calculated according to eq. (2).

earthquake. The adopted model setting (boundary conditions, loads, and fault geometry) generates dominant gravitational and tectonic forces that are compatible with the tectonic setting of Central Apennines in Italy. The applied basal shear tractions (Fig. 3) are suitable to model the large-scale interseismic displacement. These tractions allow for a first-order description of the ongoing crustal interseismic stretching of the Central Apennines and the compression of the Adriatic foreland (Figs. 1a, 4 and 5) (Barba et al., 2008; Carminati and Doglioni, 2012; Galadini et al., 2012; Carafa et al., 2015).

In the presence of crustal heterogeneities, i.e., a fault with a different shearing behaviour between its upper and lower part (Fig. 3), the concurrent action of shear tractions and the gravity force cause the normal dislocation of the unlocked portion of the fault (Fig. 6a). This generates an accumulation of interseismic stress and strain in a crustal volume at the transition between the locked and unlocked fault planes (Figs. 6b). Such stress and strain partitioning can be considered to control the activation of the seismogenic fault portion. The ongoing stretching at the brittle-plastic transition gradually increases the ΔCFS all over a volume that contains the seismogenic fault plane (Fig. 6c) until reaching the failure strength of the brittle upper part of the fault plane. Thus, in our interpretation, the existence of the basal tractions favours the occurrence of large normal-faulting earthquakes. When the failure threshold is met, the brittle part of the fault is unlocked and generates a sudden downward and SW-ward movement of the hanging wall, with a predominantly NE-ward movement of the footwall (Fig. 6d). The fault dislocation (Fig. S1) causes the hanging wall release and the reversal of the interseismic stress and strain patterns. The dilated volume, formed during the interseismic phase, shortens during the coseismic stage (Fig. 6e) and the coseismic stress increase compensates the interseismic stress relaxation at depth.

The modelled fault kinematics depends on the interseismic crustal stress and strain fields resulting from the applied boundary conditions and loads in the far-field. Such an approach differs from conventional kinematic models, where the fault mechanism is imposed by applying forces or displacements directly along the fault edges to fit geodetic or seismological data, regardless of the tectonic setting. Nevertheless, our approach is equally capable of simulating the observed coseismic scenarios. Indeed, the modelled coseismic displacements effectively reproduce the InSAR observations (Fig. 7), with residuals comparable with those obtained from kinematic models. The computed slip distribution (Fig. S1) is similar to that obtained by analytical and numerical models (Atzori et al., 2009; Trasatti et al., 2011; Castaldo et al., 2018), while the estimated geodetic moment tensor and magnitude are slightly lower than those estimated from instrumental seismicity. Such a discrepancy is related to the adopted forward modelling approach, which is not intended to search for a best-fit of the available geodetic measurements but to assess the stress and strain field before earthquake dislocation. In this sense, the obtained simple slip distribution cannot provide any clues about the source directivity or the asymmetric position of the earthquake epicentre with respect to the L'Aquila 2009 fault plane (Fig. 1b).

Both amplitude and shape of the coseismic displacement field (Fig. 6d) depend on the magnitude of applied basal shear tractions (Fig. 3), i.e., the larger the applied force is, the higher is the amplitude of the coseismic displacements. Therefore, the basal shear force can be viewed as the accumulated interseismic loading that is required to break an asperity located in the upper brittle fault portion and to generate an earthquake of a given magnitude. The shear traction amplitude depends on the assumed modelling hypotheses; thus, it cannot be interpreted in absolute terms. Nonetheless, we can analyse the time factor, i.e., approximately 1900 years, obtained by fitting the modelled interseismic horizontal displacements with the horizontal ground velocities from GPS data (Fig. 5). This time factor can be interpreted as an approximate estimate of the time required to generate an earthquake of a specified magnitude on the same fault segment. This time-factor links the coseismic displacements with the interseismic ground velocity and does not depend on the model parameters. A comparison with the literature shows that the computed time-factor resembles with the typical recurrence time interval for normal fault earthquakes in Central Italy with magnitudes ranging between 5.6 and 7.0, i.e., approximately 1200–3000 years, inferred from slip rates and average displacement measurements (DISS Working Group, 2018; Galadini and Galli, 2000; Galli et al., 2008). However, the modelled time-factor does not consider the effect of earthquake interaction, which could anticipate, but also delay, the occurrence of an earthquake on a specific fault segment by several hundred years in Central Italy, according to Wedmore et al. (2017).

The assumed abrupt transition between the shallow and deep fault planes (Fig. 3) mimics a much more complex behaviour of the shear zone. Indeed, a broad transition generally exists between the unstable and stable sliding of the fault, and between its brittle and plastic behaviour, as a function of pressure and temperature gradients and rheological parameters (see Scholz (2019) and references therein). Moreover, we assumed a finite length for the creeping fault plane (the green plane No. 1 in Fig. 3). This approximation produces numerical artefacts such as the stress and strain lobes that develop at the lower tip of the shearing fault plane (Fig. 6b and c). These lobes, which are symmetrical and opposite in sign respect to those that develop at the transition between the locked and unlocked fault planes, are caused by the assumed along-dip finite length of the fault. However, such an approximation does not affect the general validity of the obtained results.

Our modelling approach aims at assessing the long-term interseismic stress and strain pattern before an earthquake rather than analysing the trend and shape of the loading path until the earthquake nucleation. In particular, the interseismic phase simulates the accumulation of stress and strain regardless of time, neglecting the viscous-plastic behaviour of geomaterials and the coupling between the solid and fluid phase. Modelling these aspects is not straightforward since it requires knowing several parameters, such as the tectonic strain-rate and the hydraulic properties of the medium, the latter being strongly heterogeneous and anisotropic at seismogenic depth (Gleeson and Ingebritsen, 2012).

However, the proposed approach provides an overall picture of the accumulated stress and strain fields before the earthquake. In particular, the most significant results of our model are the computed volumetric strain and ΔCFS at the end of the interseismic phase (Fig. 6b and c). Interseismic volumetric strains comply with some geophysical and geodetic signals observed before the earthquake nucleation. In detail, i) the dilating and contracting volumes (Fig. 8a) roughly correspond with the volumes where respectively low and high V_p/V_s anomalies were detected before the earthquake (see Fig. 4 in Lucente et al. (2010)), and ii) the dilating volume in the hanging wall is located approximately below the Pizzoli e Preturo Quaternary basins (Fig. 8a), where accelerating ground subsidence was detected with satellite data, three years before the mainshock (see Fig. 1 in Moro et al. (2017)).

The interseismic ΔCFS pattern agrees with the spatial distribution of seismicity registered before the mainshock in the period of January–March 2009 (Chiaraluce et al., 2011) (Fig. 1b). In particular, approximately 89% of the foreshocks falls in volumes where the ΔCFS is positive (red spheres in Fig. 8b). Such a percentage increases to around 95% considering the ΔCFS on preferential NW-SE trending fault planes and dipping 50° to the NE, i.e., antithetic to the mainshock causative fault (Fig. S2), consistent with the fact that some of the foreshocks developed along a secondary antithetic fault plane (Chiaraluce et al., 2011).

These correspondences allow portraying a unified sketch of the phenomena likely occurred before the L'Aquila 2009 mainshock. During the interseismic phase, the continuous shearing of the deep fault plane (No. 1 in Fig. 3) determines the growth of dilated and compressed volumes at depth in the hanging wall and footwall, respectively, and the increase in shear stresses on the mainshock causative fault and secondary antithetic planes (Fig. 6c and Fig. S2). The progressive

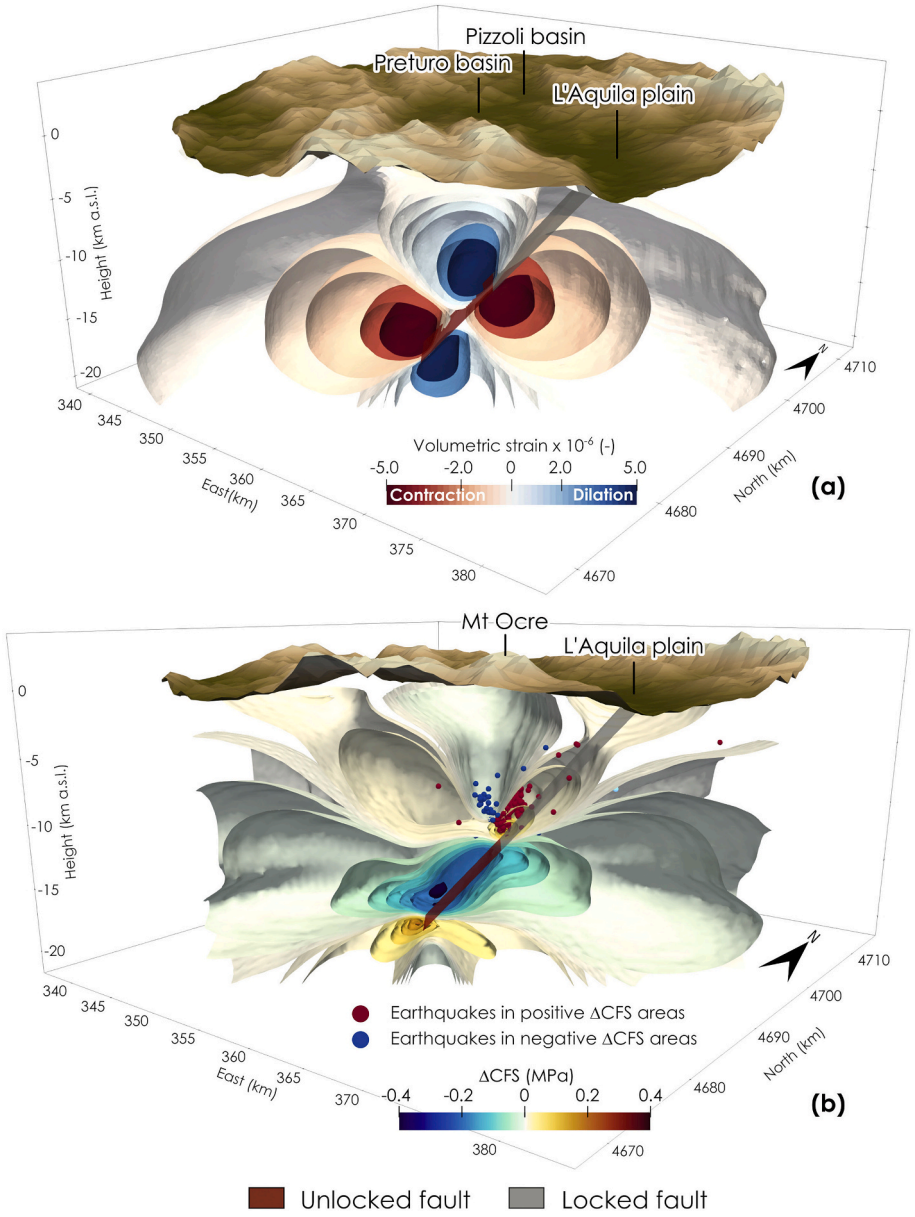

Fig. 8. 3D sketch showing a) the location of the computed dilated and contracted volumes and b) the ΔCFS at the end of the interseismic phase calculated along NW-SE trending fault planes dipping 47° towards SW. The red and blue spheres in panel b identify the foreshocks location (from Valoroso et al., 2013) in positive and negative ΔCFS volumes, respectively. (For interpretation of the references to colour in this figure legend, the reader is referred to the web version of this article.)

accumulation of dilatancy and shear stresses presupposes crack growth by tensile-opening and in-plane shear fractures in the hanging wall (Scholz, 2019), which triggered foreshocks (Chiaraluce et al., 2011). The latter developed from January 2009, with an increasing seismicity rate and a decreasing b-value (Gulia et al., 2016; Sugan et al., 2014). Foreshocks were also accompanied by slow slip events (Borghi et al., 2016) that reflect the progressive stress increase on synthetic and antithetic planes surrounding an impending rupture zone (Fig. 8b), caused by the differential slip behaviour of the brittle and plastic fault planes (Sugan et al., 2014).

In the presence of voids filled with fluids (Fyfe, 2012), volumetric changes imply a variation in the void space of the solid and a contextual modification in the fluid pore pressures respect to the hydrostatic, especially in case of the presence of low permeability strata (Lucente et al., 2010; Doglioni et al., 2014). Thus, two different compartments develop; one of dilatant material in the hanging wall block, filled with pore fluids at sub-hydrostatic pressure and another one of contracted material in the footwall block, filled with highly pressurized fluid, with the fault acting as an impermeable seal separating them (Fig. 8a) (Bense et al., 2013; Lucente et al., 2010). This scenario explains the low and high V_P/V_S ratios detected in the hanging wall and footwall, respectively (Lucente et al., 2010; Terakawa et al., 2010). Pore pressure gradients could trigger fluid flow into the hanging wall volume from deep overpressurized CO_2 rich zones, as postulated by Chiodini et al. (2004). If the fluid diffusion is steady, it could affect the surficial phreatic aquifers inside Quaternary basins, thus lowering the groundwater table and causing soil consolidation, as observed in the Preturo and Pizzoli basins (Moro et al., 2017), which are located in the hanging wall and approximately above the dilated volume (Fig. 8a). Otherwise, the diffusion could be abrupt because of the rupture of a permeability barrier, as supposed by Lucente et al. (2010) after the nucleation of the 30 March 2009, M_w 4.0 foreshock. This event could lead to a fluid pressure pulse from the contracted volume of the footwall into the dilated volume of the hanging wall, thus explaining the observed sharp changes in the $V_P/$

V_S ratio in the hanging wall and footwall observed one week before the mainshock (Baccheschi et al., 2019; Lucente et al., 2010), the concurrent abrupt modifications of seismicity rate and b-value (Gulia et al., 2016), and the triggering of the mainshock.

5. Conclusions

The results of the performed numerical model provide a quantitative description of the interseismic stress and strain pattern at seismogenic depth before the earthquake nucleation along normal faults as proposed by Bignami et al. (2020). Modelling of the interseismic phase shows evidence of interseismic dilatancy at depth in the hanging wall, in a volume embedding the L'Aquila 2009 earthquake hypocentre, while volumetric contraction develops in the footwall. Such volumetric changes provide a quantitative description of the geophysical and geodetic signals observed before the mainshock, i.e., the V_p/V_s anomalies and the ground subsidence observed with satellite data. Moreover, the partitioning of the interseismic ΔCFS stress at the transition between the brittle and plastic fault segments promotes the coseismic dislocation of the hanging wall and agrees with the spatial distribution of foreshocks detected before the mainshock nucleation.

The modelled interseismic stress and strain patterns invert during the coseismic stage. The dilated volume, formed during the interseismic phase, will be contracted and, conversely, the volume in the footwall that was previously contracted will be expanded.

Data availability

The results of the numerical model, expressed in terms of nodal stresses, strains and displacements, are available at the following link: doi:https://doi.org/10.5281/zenodo.3950811, a data repository hosted at www.zenodo.org.

Declaration of Competing Interest

The authors declare that they have no known competing financial interests or personal relationships that could have appeared to influence the work reported in this paper.

Acknowledgements

We thank R. Devoti and L. Valoroso for providing the GPS interseismic horizontal velocities of the Italian territory and the seismic data for the L'Aquila 2009 event. We thank the European Space Agency (ESA) for providing the ENVISAT SAR data. Figures are made with the freely available codes Paraview 5.8.1 (https://www.paraview.org/), QGIS 3.10 (https://www.qgis.org/it/site/) and Veusz 3.2 (https://veusz.github.io/). The scientific colour maps (Crameri, 2018) are used in specific figures to prevent visual distortion of the data and exclusion of readers with colour-vision deficiencies.

Appendix A. Supplementary data

Supplementary data to this article can be found online at https://doi.org/10.1016/j.tecto.2020.228685.

References

Aharonov, E., Scholz, C.H., 2018. A physics-based rock friction constitutive law: steady state friction. J. Geophys. Res. Solid Earth 123, 1591–1614. https://doi.org/10.1002/2016JB013829.

Albano, M., Barba, S., Saroli, M., Moro, M., Malvarosa, F., Costantini, M., Bignami, C., Stramondo, S., 2015. Gravity-driven postseismic deformation following the Mw 6.3 2009 L'Aquila (Italy) earthquake. Sci. Rep. 5, 16558. https://doi.org/10.1038/srep16558.

Amato, A., Montone, P., 1997. Present-day stress field and active tectonics in southern peninsular Italy. Geophys. J. Int. 130, 519–534. https://doi.org/10.1111/j.1365-246X.1997.tb05666.x.

Atzori, S., Hunstad, I., Chini, M., Salvi, S., Tolomei, C., Bignami, C., Stramondo, S., Trasatti, E., Antonioli, A., Boschi, E., 2009. Finite fault inversion of DInSAR coseismic displacement of the 2009 L'Aquila earthquake (Central Italy). Geophys. Res. Lett. 36 https://doi.org/10.1029/2009GL039293.

Atzori, S., Chiarabba, C., Devoti, R., Bonano, M., Lanari, R., 2013. Anomalous far-field geodetic signature related to the 2009 L'Aquila (central Italy) earthquake. Terra 343–351. https://doi.org/10.1111/ter.12040, 25 November.

Baccheschi, P., De Gori, P., Villani, F., Trippetta, F., Chiarabba, C., 2019. The preparatory phase of the Mw 6.1 2009 L'Aquila (Italy) normal faulting earthquake traced by foreshock time-lapse tomography. Geology 48, 49–55. https://doi.org/10.1130/G46618.1.

Barba, S., Carafa, M.M.C., Boschi, E., 2008. Experimental evidence for mantle drag in the Mediterranean. Geophys. Res. Lett. 35, 1–6. https://doi.org/10.1029/2008GL033281.

Barba, S., Carafa, M.M.C., Mariucci, M.T., Montone, P., Pierdominici, S., 2010. Present-day stress-field modelling of southern Italy constrained by stress and GPS data. Tectonophysics 482, 193–204. https://doi.org/10.1016/J.TECTO.2009.10.017.

Bense, V.F., Gleeson, T., Loveless, S.E., Bour, O., Scibek, J., 2013. Fault zone hydrogeology. Earth-Sci. Rev. 127, 171–192. https://doi.org/10.1016/j.earscirev.2013.09.008.

Bignami, C., Valerio, E., Carminati, E., Doglioni, C., Tizzani, P., Lanari, R., 2019. Volume unbalance on the 2016 Amatrice - Norcia (Central Italy) seismic sequence and insights on normal fault earthquake mechanism. Sci. Rep. 9, 4250. https://doi.org/10.1038/s41598-019-40958-z.

Bignami, C., Valerio, E., Carminati, E., Doglioni, C., Petricca, P., Tizzani, P., Lanari, R., 2020. Are normal fault earthquakes due to elastic rebound or gravitational collapse? Ann. Geophys. 63 (2) https://doi.org/10.4401/ag-8455. SE213, 2020.

Borghi, A., Aoudia, A., Javed, F., Barzaghi, R., 2016. Precursory slow-slip loaded the 2009 L'Aquila earthquake sequence. Geophys. J. Int. 205, 776–784. https://doi.org/10.1093/gji/ggw046.

Bouchon, M., Durand, V., Marsan, D., Karabulut, H., Schmittbuhl, J., 2013. The long precursory phase of most large interplate earthquakes. Nat. Geosci. 6, 299–302. https://doi.org/10.1038/ngeo1770.

Byerlee, J., 1978. Friction of rocks. Pure Appl. Geophys. 116, 615–626. https://doi.org/10.1007/BF00876528.

Candela, S., Mazzoli, S., Megna, A., Santini, S., 2015. Finite element modelling of stress field perturbations and interseismic crustal deformation in the Val d'Agri region, southern Apennines, Italy. Tectonophysics 657, 245–259. https://doi.org/10.1016/J.TECTO.2015.07.011.

Carafa, M.M.C., Bird, P., 2016. Improving deformation models by discounting transient signals in geodetic data: 2. Geodetic data, stress directions, and long-term strain rates in Italy. J. Geophys. Res. Solid Earth 121, 5557–5575. https://doi.org/10.1002/2016JB013038.

Carafa, M.M.C., Barba, S., Bird, P., 2015. Neotectonics and long-term seismicity in Europe and the Mediterranean region. J. Geophys. Res. Solid Earth 120, 5311–5342. https://doi.org/10.1002/2014JB011751.

Carannante, S., Monachesi, G., Cattaneo, M., Amato, A., Chiarabba, C., 2013. Deep structure and tectonics of the northern-central Apennines as seen by regional-scale tomography and 3-D located earthquakes. J. Geophys. Res. Solid Earth 118, 5391–5403. https://doi.org/10.1002/jgrb.50371.

Carminati, E., Doglioni, C., 2012. Alps vs. Apennines: the paradigm of a tectonically asymmetric Earth. Earth-Sci. Rev. 112, 67–96. https://doi.org/10.1016/J.EARSCIREV.2012.02.004.

Castaldo, R., de Nardis, R., DeNovellis, V., Ferrarini, F., Lanari, R., Lavecchia, G., Pepe, S., Solaro, G., Tizzani, P., 2018. Coseismic stress and Strain field changes investigation through 3-D finite element modeling of DInSAR and GPS measurements and geological/seismological data: the L'Aquila (Italy) 2009 earthquake case study. J. Geophys. Res. Solid Earth 123, 4193–4222. https://doi.org/10.1002/2017JB014453.

Chiarabba, C., De Gori, P., Mele, F.M., 2015. Recent seismicity of Italy: active tectonics of the Central Mediterranean region and seismicity rate changes after the Mw 6.3 L'Aquila earthquake. Tectonophysics 638, 82–93. https://doi.org/10.1016/j.tecto.2014.10.016.

Chiaraluce, L., Chiarabba, C., De Gori, P., Di Stefano, R., Improta, L., Piccinini, D., Schlagenhauf, A., Traversa, P., Valoroso, L., Vosin, C., 2011. The 2009 L'Aquila (Central Italy) seismic sequence. Boll. Geofis. Teor. Appl. 52, 367–387.

Chiodini, G., Cardellini, C., Amato, A., Boschi, E., Caliro, S., Frondini, F., Ventura, G., 2004. Carbon dioxide Earth degassing and seismogenesis in central and southern Italy. Geophys. Res. Lett. 31, 2–5. https://doi.org/10.1029/2004GL019480.

Cicerone, R.D., Ebel, J.E., Britton, J., 2009. A systematic compilation of earthquake precursors. Tectonophysics 476, 371–396. https://doi.org/10.1016/J.TECTO.2009.06.008.

Costantini, M., 1998. A novel phase unwrapping method based on network programming. IEEE Trans. Geosci. Remote Sens. 36, 813–821. https://doi.org/10.1109/36.673674.

Crameri, F., 2018. Scientific colour-maps. https://doi.org/10.5281/ZENODO.1287763.

Crampin, S., Gao, Y., Bukits, J., 2015. A review of retrospective stress-forecasts of earthquakes and eruptions. Phys. Earth Planet. Inter. 245, 76–87. https://doi.org/10.1016/j.pepi.2015.05.008.

Cuffaro, M., Riguzzi, F., Scrocca, D., Antonioli, F., Carminati, E., Livani, M., Doglioni, C., 2010. On the geodynamics of the northern Adriatic plate. Rend. LINCEI 21, 253–279. https://doi.org/10.1007/s12210-010-0098-9.

De Gori, P., Lucente, F.P., Lombardi, A.M., Chiarabba, C., Montuori, C., 2012. Heterogeneities along the 2009 L'Aquila normal fault inferred by the b-value distribution. Geophys. Res. Lett. 39, 1–5. https://doi.org/10.1029/2012GL052822.

Devoti, R., D'Agostino, N., Serpelloni, E., Pietrantonio, G., Riguzzi, F., Avallone, A., Cavaliere, A., Cheloni, D., Cecere, G., D'Ambrosio, C., Franco, L., Selvaggi, G., Metois, M., Esposito, A., Sepe, V., Galvani, A., Anzidei, M., 2017. A combined velocity field of the mediterranean region. Ann. Geophys. 60, S0215. https://doi.org/10.4401/ag-7059.

Di Luccio, F., Ventura, G., Di Giovambattista, R., Piscini, A., Cinti, F.R., 2013. Erratum: Normal faults and thrusts reactivated by deep fluids: The 6 April 2009 Mw 6.3 L'Aquila earthquake, central Italy. J. Geophys. Res. Solid Earth 115 (B06315). https://doi.org/10.1029/2009JB007190 (2010). 118, 5596. doi:10.1002/jgrb.50369.

Di Toro, G., Han, R., Hirose, T., De Paola, N., Nielsen, S., Mizoguchi, K., Ferri, F., Cocco, M., Shimamoto, T., 2011. Fault lubrication during earthquakes. Nature 471, 494–498. https://doi.org/10.1038/nature09838.

DISS Working Group, 2018. Database of Individual Seismogenic sources (DISS), Version 3.2.1: a compilation of potential sources for earthquakes larger than M 5.5 in Italy and surrounding areas. Ist. Naz. di Geofis. e Vulcanol. https://doi.org/10.6092/INGV.IT-DISS3.2.1.

Doglioni, C., 1991. A proposal of kinematic modelling for W-dipping subductions - possible applications to the Tyrrhenian - Apennines system. Terra Nova 3 (4), 423–434.

Doglioni, C., Gueguen, E., Harabaglia, P., Mongelli, F., 1999. On the origin of west-directed subduction zones and applications to the western Mediterranean. Geol. Soc. Spec. Publ. 156, 541–561. https://doi.org/10.1144/GSL.SP.1999.156.01.24.

Doglioni, C., Barba, S., Carminati, E., Riguzzi, F., 2011. Role of the brittle-ductile transition on fault activation. Phys. Earth Planet. Inter. 184, 160–171. https://doi.org/10.1016/j.pepi.2010.11.005.

Doglioni, C., Barba, S., Carminati, E., Riguzzi, F., 2014. Fault on–off versus coseismic fluids reaction. Geosci. Front. 5, 767–780. https://doi.org/10.1016/j.gsf.2013.08.004.

Doglioni, C., Carminati, E., Petricca, P., Riguzzi, F., 2015. Normal fault earthquakes or graviquakes. Sci. Rep. 5, 12110. https://doi.org/10.1038/srep12110.

Falcucci, E., Gori, S., Peronace, E., Fubelli, G., Moro, M., Saroli, M., Giaccio, B., Messina, P., Naso, G., Scardia, G., Sposato, A., Voltaggio, M., Galli, P., Galadini, F., 2009. The paganica fault and surface coseismic ruptures caused by the 6 April 2009 earthquake (L'Aquila, central Italy). Seismol. Res. Lett. 80, 940–950. https://doi.org/10.1785/gssrl.80.6.940.

Farr, T.G., Rosen, P.A., Caro, E., Crippen, R., Duren, R., Hensley, S., Kobrick, M., Paller, M., Rodriguez, E., Roth, L., Seal, D., Shaffer, S., Shimada, J., Umland, J., Werner, M., Oskin, M., Burbank, D., Alsdorf, D., 2007. The shuttle radar topography mission. Rev. Geophys. 45, RG2004 https://doi.org/10.1029/2005RG000183.

Ferranti, L., Oldow, J.S., 1999. History and tectonic implications of low-angle detachment faults and orogen parallel extension, Picentini Mountains, Southern Apennines fold and thrust belt, Italy. Tectonics 18, 498–526. https://doi.org/10.1029/1998TC900024.

Finocchio, D., Barba, S., Santini, S., Megna, A., 2013. Interpreting the interseismic deformation of the Altotiberina fault (Central Italy) through 2D modelling. Ann. Geophys. 56 https://doi.org/10.4401/ag-5806.

Finocchio, D., Barba, S., Basili, R., 2016. Slip rate depth distribution for active faults in Central Italy using numerical models. Tectonophysics 687, 232–244. https://doi.org/10.1016/j.tecto.2016.07.031.

Fyfe, W.S., 2012. Fluids in the Earth's Crust: Their Significance in Metamorphic, Tectonic and Chemical Transport Process, Developments in Geochemistry. Elsevier Science.

Galadini, F., Galli, P., 2000. Active tectonics in the Central Appennines (Italy) - Input data for seismic hazard assessment. Nat. Hazards 22, 225–268. https://doi.org/10.1023/A:1008149531980.

Galadini, F., Falcucci, E., Galli, P., Giaccio, B., Gori, S., Messina, P., Moro, M., Saroli, M., Scardia, G., Sposato, A., 2012. Time intervals to assess active and capable faults for engineering practices in Italy. Eng. Geol. 139–140, 50–65. https://doi.org/10.1016/j.enggeo.2012.03.012.

Galli, P., Galadini, F., Pantosti, D., 2008. Twenty years of paleoseismology in Italy. Earth-Science Rev. 88, 89–117. https://doi.org/10.1016/j.earscirev.2008.01.001.

Gleeson, T., Ingebritsen, S., 2012. Crustal Permeability. John Wiley & Sons, Ltd, Chichester, UK. https://doi.org/10.1002/9781119166573.

Goldstein, R.M., Werner, C.L., 1998. Radar interferogram filtering for geophysical applications. Geophys. Res. Lett. 25, 4035–4038. https://doi.org/10.1029/1998GL900033.

Gori, S., Falcucci, E., Atzori, S., Chini, M., Moro, M., Serpelloni, E., Fubelli, G., Saroli, M., Devoti, R., Stramondo, S., Galadini, F., Salvi, S., 2012. Constraining primary surface rupture length along the Paganica fault (2009 L'Aquila earthquake) with geological and geodetic (DInSAR and GPS) data. Ital. J. Geosci. 131, 359–372. https://doi.org/10.3301/IJG.2012.21.

Gulia, L., Tormann, T., Wiemer, S., Herrmann, M., Seif, S., 2016. Short-term probabilistic earthquake risk assessment considering time-dependent b values. Geophys. Res. Lett. 43, 1100–1108. https://doi.org/10.1002/2015GL066686.

Hartmann, J., Levy, J.K., 2005. Hydrogeological and gasgeochemical earthquake precursors - a review for application. Nat. Hazards. https://doi.org/10.1007/s11069-004-2072-2.

Hippolyte, J.C., Angelier, J., Roure, F., 1994. A major geodynamic change revealed by Quaternary stress patterns in the southern Apennines (Italy). Tectonophysics 230, 199–210. https://doi.org/10.1016/0040-1951(94)90135-X.

Kastelic, V., Carafa, M.M.C., 2012. Fault slip rates for the active external dinarides thrust-and-fold belt. Tectonics 31. https://doi.org/10.1029/2011TC003022.

Lavecchia, G., Adinolfi, G.M., de Nardis, R., Ferrarini, F., Cirillo, D., Brozzetti, F., De Matteis, R., Festa, G., Zollo, A., 2017. Multidisciplinary inferences on a newly recognized active east-dipping extensional system in Central Italy. Terra Nov. 29, 77–89. https://doi.org/10.1111/ter.12251.

Livani, M., Scrocca, D., Arecco, P., Doglioni, C., 2018. Structural and stratigraphic control on salient and recess development along a thrust belt front: the Northern Apennines (Po Plain, Italy). J. Geophys. Res. Solid Earth 123, 4360–4387. https://doi.org/10.1002/2017JB015235.

Lucente, F.P., De Gori, P., Margheriti, L., Piccinini, D., Di Bona, M., Chiarabba, C., Piana Agostinetti, N., 2010. Temporal variation of seismic velocity and anisotropy before the 2009 M W 6.3 L'Aquila earthquake, Italy. Geology 38, 1015–1018. https://doi.org/10.1130/G31463.1.

Malinverno, A., Ryan, W.B.F., 1986. Extension in the Tyrrhenian Sea and shortening in the Apennines as result of arc migration driven by sinking of the lithosphere. Tectonics 5, 227–245. https://doi.org/10.1029/TC005i002p00227.

Massonnet, D., Feigl, K.L., 1998. Radar interferometry and its application to changes in the Earth's surface. Rev. Geophys. 36, 441–500. https://doi.org/10.1029/97RG03139.

Mavrommatis, A.P., Segall, P., Johnson, K.M., 2014. A decadal-scale deformation transient prior to the 2011 M w 9.0 Tohoku-oki earthquake. Geophys. Res. Lett. 41, 4486–4494. https://doi.org/10.1002/2014GL060139.

Moro, M., Saroli, M., Stramondo, S., Bignami, C., Albano, M., Falcucci, E., Gori, S., Doglioni, C., Polcari, M., Tallini, M., Macerola, L., Novali, F., Costantini, M., Malvarosa, F., Wegmüller, U., 2017. New insights into earthquake precursors from InSAR. Sci. Rep. 7, 12035. https://doi.org/10.1038/s41598-017-12058-3.

MSC Software Corporation, 2018. Marc 2018.1 Volume A: Theory and User Information [WWW Document]. URL. http://www.mscsoftware.com/it/product/marc (accessed 3.16.18).

Nur, A., 1972. Dilatancy, pore fluids, and premonitory variations of ts/tp travel times. Bull. Seismol. Soc. Am. 62, 1217–1222.

Ohtake, M., Matumoto, T., Latham, G.V., 1981. Evaluation of the forecast of the 1978 Oaxaca, southern Mexico earthquake based on a precursory seismic quiescence. Earthq. Predict. An Int. Rev. 53–61. https://doi.org/10.1029/me004p0053.

Palano, M., 2015. On the present-day crustal stress, strain-rate fields and mantle anisotropy pattern of Italy. Geophys. J. Int. 200, 969–985. https://doi.org/10.1093/gji/ggu451.

Patacca, E., Sartori, R., Scandone, P., 1990. Tyrrhenian basin and Apenninic arcs: kinematic relations since late Tortonian times. Mem. Soc. Geol. Ital. 45, 425–451.

Petricca, P., Barba, S., Carminati, E., Doglioni, C., Riguzzi, F., 2015. Graviquakes in Italy. Tectonophysics. https://doi.org/10.1016/j.tecto.2015.07.001.

Pezzo, G., Petracchini, L., Devoti, R., Maffucci, R., Anderlini, L., Antoncecchi, I., Billi, A., Carminati, E., Ciccone, F., Cuffaro, M., Livani, M., Palano, M., Petricca, P., Pietrantonio, G., Riguzzi, F., Rossi, G., Sparacino, F., Doglioni, C., 2020. Active fold-thrust belt to foreland transition in northern Adria, Italy, tracked by seismic reflection profiles and GPS offshore data. Tectonics 39 (11). https://doi.org/10.1029/2020TC006425.

Roeloffs, E.A., 1988. Hydrologic precursors to earthquakes: a review. Pure Appl. Geophys. PAGEOPH 126, 177–209. https://doi.org/10.1007/BF00878996.

Ruina, A., 1983. Slip instability and state variable friction laws. J. Geophys. Res. Solid Earth 88, 10359–10370. https://doi.org/10.1029/JB088iB12p10359.

Savage, M.K., 2010. The role of fluids in earthquake generation in the 2009 Mw 6.3 L'Aquila, Italy, earthquake and its foreshocks. Geology 38, 1055–1056. https://doi.org/10.1130/focus112010.1.

Scholz, C.H., 1974. Post-Earthquake Dilatancy Recovery. Geology 2, 551. https://doi.org/10.1130/0091-7613(1974)2<551:PDR>2.0.CO;2.

Scholz, C.H., 2019. The Mechanics of Earthquakes and Faulting. Cambridge University Press. https://doi.org/10.1017/9781316681473.

Schurr, B., Asch, G., Hainzl, S., Bedford, J., Hoechner, A., Palo, M., Wang, R., Moreno, M., Bartsch, M., Zhang, Y., Oncken, O., Tilmann, F., Dahm, T., Victor, P., Barrientos, S., Vilotte, J.P., 2014. Gradual unlocking of plate boundary controlled initiation of the 2014 Iquique earthquake. Nature 512, 299–302. https://doi.org/10.1038/nature13681.

Serpelloni, E., Anderlini, L., Belardinelli, M.E., 2012. Fault geometry, coseismic-slip distribution and Coulomb stress change associated with the 2009 6 April, Mw 6.3, L'Aquila earthquake from inversion of GPS displacements. Geophys. J. Int. 188, 473–489. https://doi.org/10.1111/j.1365-246X.2011.05279.x.

Sugan, M., Kato, A., Miyake, H., Nakagawa, S., Vuan, A., 2014. The Preparatory Phase of the 2009 Mw 6.3L'Aquila Earthquake by Improving the Detection Capability of Low-Magnitude Foreshocks, pp. 6137–6144. https://doi.org/10.1002/2014GL061199. Received.

Terakawa, T., Zoporowski, A., Galvan, B., Miller, S.A., 2010. High-pressure fluid at hypocentral depths in the L'Aquila region inferred from earthquake focal mechanisms. Geology 38, 995–998. https://doi.org/10.1130/G31457.1.

Trasatti, E., Kyriakopoulos, C., Chini, M., 2011. Finite element inversion of DInSAR data from the Mw 6.3 L'Aquila earthquake, 2009 (Italy). Geophys. Res. Lett. 38 https://doi.org/10.1029/2011GL046714 n/a-n/a.

Tung, S., Masterlark, T., 2018. Resolving source geometry of the 24 August 2016 Amatrice, Central Italy, earthquake from InSAR Data and 3D finite-element modeling. Bull. Seismol. Soc. Am. 108, 553–572. https://doi.org/10.1785/0120170139.

Valoroso, L., Chiaraluce, L., Piccinini, D., Di Stefano, R., Schaff, D., Waldhauser, F., 2013. Radiography of a normal fault system by 64,000 high-precision earthquake locations: the 2009 L'Aquila (Central Italy) case study. J. Geophys. Res. Solid Earth 118, 1156–1176. https://doi.org/10.1002/jgrb.50130.

Volpe, M., Piersanti, A., Melini, D., 2012. Complex 3-D Finite Element modelling of the 2009 6 April L'Aquila earthquake by inverse analysis of static deformation. Geophys. J. Int. 188, 1339–1358. https://doi.org/10.1111/j.1365-246X.2011.05330.x.

Wedmore, L.N.J., Faure Walker, J.P., Roberts, G.P., Sammonds, P.R., McCaffrey, K.J.W., Cowie, P.A., 2017. A 667 year record of coseismic and interseismic Coulomb stress changes in Central Italy reveals the role of fault interaction in controlling irregular

earthquake recurrence intervals. J. Geophys. Res. Solid Earth 122, 5691–5711. https://doi.org/10.1002/2017JB014054.
Wegmuller, U., Werner, C., Strozzi, T., 1998. SAR interferometric and differential interferometric processing chain. In: IGARSS '98. Sensing and Managing the Environment. 1998 IEEE International Geoscience and Remote Sensing. Symposium Proceedings. (Cat. No.98CH36174), vol. 2. IEEE, pp. 1106–1108. https://doi.org/10.1109/IGARSS.1998.699687.
Westaway, R., 1990. Block rotation in western Turkey 1. Observational evidence. J. Geophys. Res. 95, 19857–19884. https://doi.org/10.1029/jb095ib12p19857.